Geophysical Research Letters

Supporting Information for

Electromagnetic evidence for volatile-rich upwelling beneath the Society hotspot, French Polynesia

Noriko Tada[1], Pascal Tarits[2], Kiyoshi Baba[3], Hisashi Utada[3], Takafumi Kasaya[1], and Daisuke Suetsugu[1]

[1]Japan Agency for Marine-Earth Science and Technology, Yokosuka, Japan
[2]UMR-Domaines Océaniques, Institut Universitaire Européen de la Mer, Plouzane, France
[3]Earthquake Research Institute, The University of Tokyo, Tokyo, Japan

Contents of this file

Text S1 to S3
Figures S1 to S3
Tables S1 to S3

Introduction

This supporting information provides details of three-dimensional inversion analysis, F-test, and calculation of melt fraction and H_2O and CO_2 contents.

Text S1. Three-dimensional inversion analysis

The 3-D inversion scheme applied in this study is a regularized inversion with special treatment of seafloor topography [*Baba et al.*, 2013; *Siripunvaraporn et al.*, 2005; *Tada et al.*, 2012]. We inverted the full MT impedance tensors (2nd order complex-valued) of 17 periods between 640 and 163,840 s so that the total number of data is 2,720. The model dimensions are 8,720 km × 8,720 km × 1,057 km (75 × 75 × 58 numerical blocks). Local small-scale topographic effects that are too small to be expressed by the numerical blocks in the model were separately simulated in a small model domain for the initial 1-D model (the TIARES profile; Figure 2a) and were input in the inversion as a site-correction term [*Baba et al.*, 2013]. We ran the inversion for many cycles to update the initial and prior models, error floors, and site-correction term. Figure S2 presents changes in the RMS data misfit between observed and modelled MT responses with the inversion iterations at each cycle. The error floors of the off-diagonal elements of the MT impedance were set at 2.5% throughout all cycles. The error floors of the diagonal elements were set at 25.0% from the first to third cycle and were reduced to 5.0% at the fourth cycle and thereafter.

The site-correction term caused by local topographic distortion was updated once at the sixth cycle to reevaluate the mutual coupling between the topography and subsurface structure using the 3-D model obtained from the previous inversion cycle. The inversion was converged at the fifth iteration of the eighth cycle, and the inverted model was adopted as the image of the upper mantle beneath the study area. Figure S3 shows 3-D inversion model fits to observations.

Text S2. F-test

We carried out a one-sided *F*-test to investigate whether the current data set can distinguish the presence of the conductivity anomaly. The test statistic *F* is defined as

$$F = \frac{S_X^2}{S_Y^2}, \tag{S1}$$

where X and Y represent the modified and original models, respectively. The variance S_i^2 in Eq. (S1) is calculated as

$$S_i^2 = RMS_i^2 \times df_i, \tag{S2}$$

where i denotes X or Y, RMS_i is the RMS data misfit and df_i is the degree of freedom, which is the number of data (2,720 in this case). The null hypothesis is $S_X^2 = S_Y^2$. The alternative hypothesis is $S_X^2 > S_Y^2$, and the null hypothesis is rejected at the 5% significance level (95% acceptance level) if $F > F_{0.95}$, where $F_{0.95}$ is 95% point of the upper probability of the F-distribution.

The modified model was created by setting all electrical conductivity values greater than 0.03 S/m to be 0.03 S/m, and MT responses for these models were calculated. Calculated RMS data misfits, variances, and F statistics for these models are provided in Table S2, which shows the null hypothesis (the electrical conductivity anomaly of Zone A is insignificant) can be rejected at 95% confidence level.

Text S3. Calculation of melt fraction and H_2O and CO_2 contents

The stable melt mass fraction and H_2O and CO_2 contents in melt and olivine were obtained for arbitrary temperature, with the contents of H_2O and CO_2 in bulk mantle incorporating for the solidus reduction due to H_2O and CO_2 and partitioning of these volatiles based on equations proposed by Hirschmann [*Hirschmann*, 2010]. However, we applied alternative values for: 1) a freezing-point depression caused by CO_2 [*Dasgupta et al.*, 2013], interpolating their experimental data at 2, 3, 4, and 5 GPa into arbitrary pressure; 2) the upper limit of concentration of CO_2 in partial melts is set to be 40 wt.%, because carbonated peridotite melts will be saturated with CO_2 at about 40 wt.% to form carbonatite melts

3

[*Dasgupta* et al., 2007]; 3) a partition coefficient of CO_2 between peridotite and melt of 0.0001 was used [*Dasgupta et al.*, 2007]; and 4) partition coefficients of H_2O between peridotite and melt and between olivine and melt [*Sifré et al.*, 2014].

 The bulk electrical conductivity was calculated depending on the volume fraction of the melt. In the case that the calculated melt fraction is zero, the bulk electrical conductivity is considered to be equal to the electrical conductivity of olivine. The electrical conductivity of olivine was calculated using an empirical law [*Gardés et al.*, 2014] as a function of temperature and H_2O content in olivine. In the case where the calculated melt fraction is greater than zero, the bulk electrical conductivity is calculated as mixing of the electrical conductivity values of olivine and melt, using Hashin–Shtrikman upper and lower bounds for interconnected and isolated melt cases, respectively [*Hashin and Shtrikman*, 1962]. In this study, we adopted the upper bound for calculating the bulk electrical conductivity whose melt fraction is greater than 0.0002 wt% [*Minarik and Watson*, 1995]. The electrical conductivity of melt was calculated using Eq. (1) of Sifré et al. [*Sifré et al.*, 2014] as a function of temperature and the H_2O and CO_2 content in the melt.
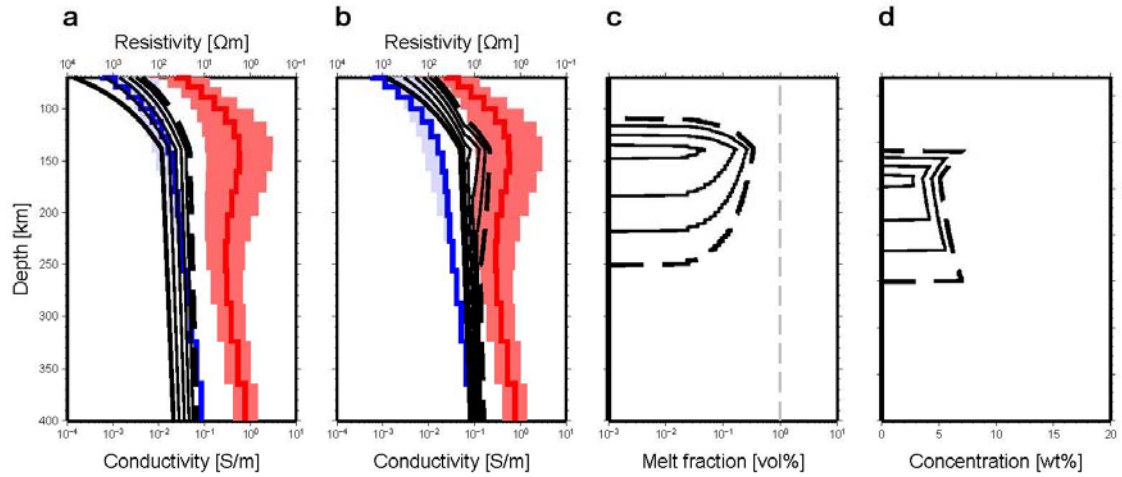
Figure S1. Electrical conductivity explained by including only H_2O. (a) Calculated electrical conductivities assuming a geotherm by the plate cooling model when the bulk CO_2 content is zero, changing the bulk H_2O contents from 0 (black solid line) to 500 ppmw (thick black dashed solid line) with 100 ppmw increments. Red and blue colors denote the averaged 1-D electrical conductivities for Zone A and the TIARES region, respectively. In these cases, the melt fraction and H_2O content in melt are zero over the whole depth range.

(b) Calculated electrical conductivities, (c) melt fraction, and (d) H_2O content in melt in the case where the temperature is higher by 200 °C than the plate cooling model.
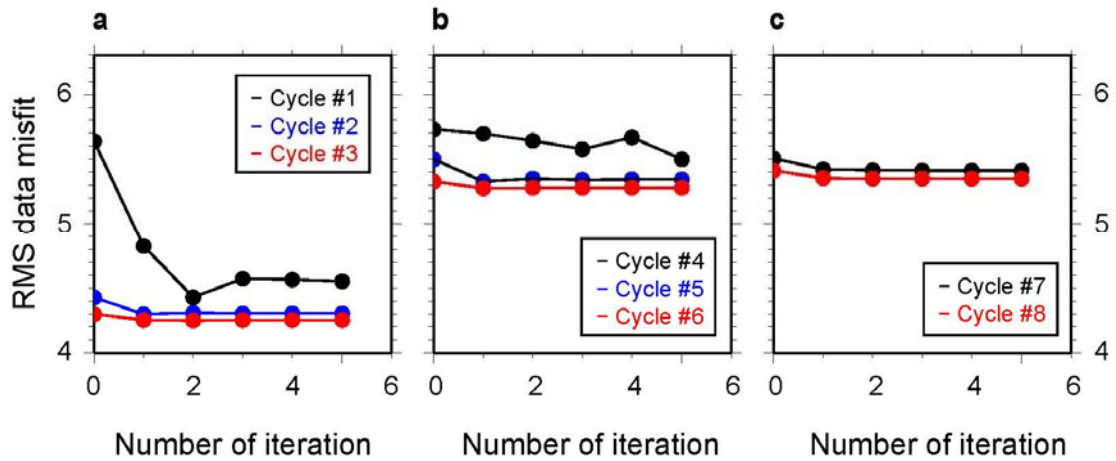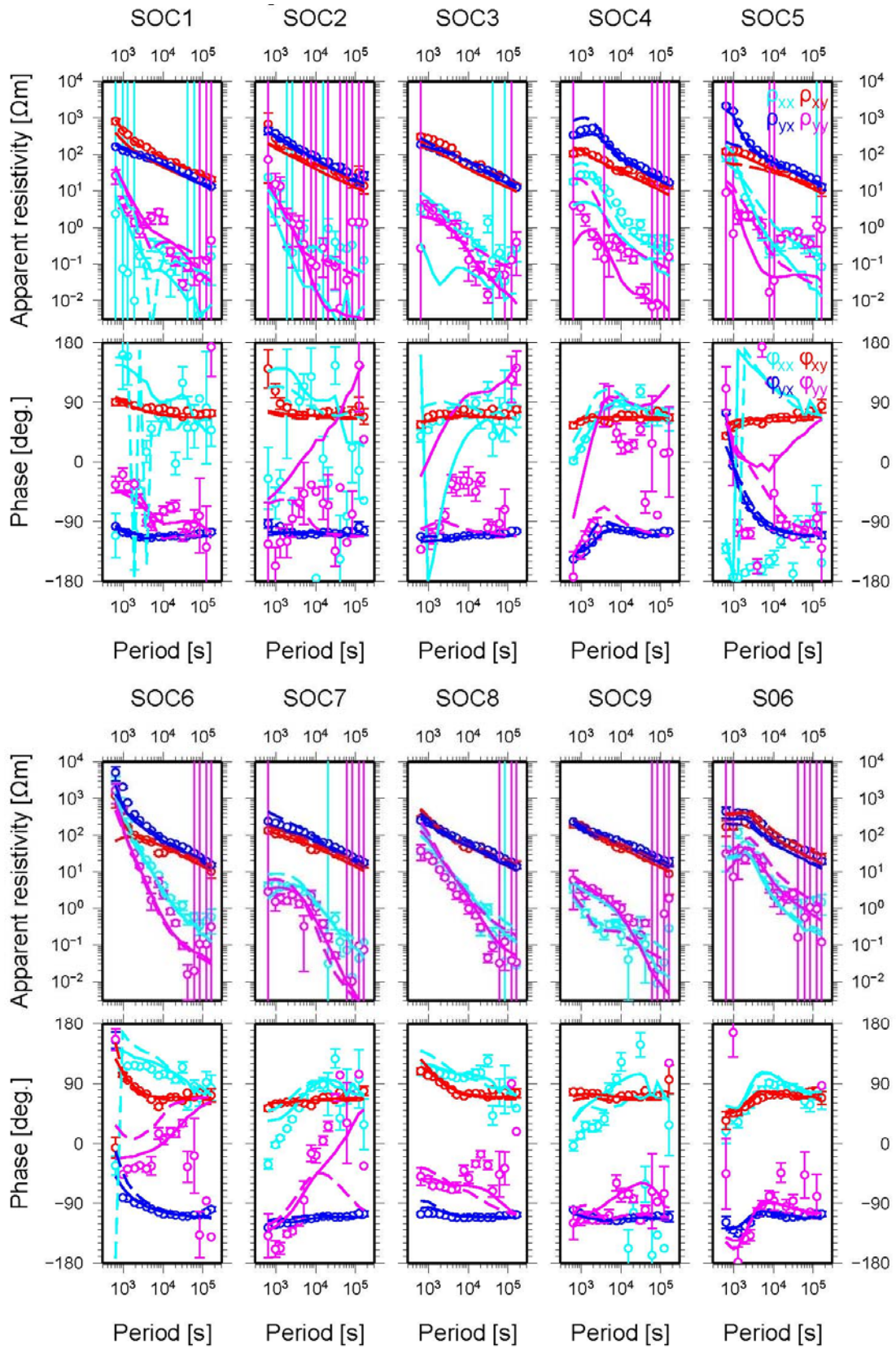

Figure S2. RMS data misfit. (a) Variations of the RMS data misfit when the error floors of the diagonal elements were set at 25.0%. (b) Variations of the RMS data misfit after the error floors of the diagonal elements were reduced to 5.0%. (c) Variations of the RMS data misfit after the local topographic distortion was reevaluated.
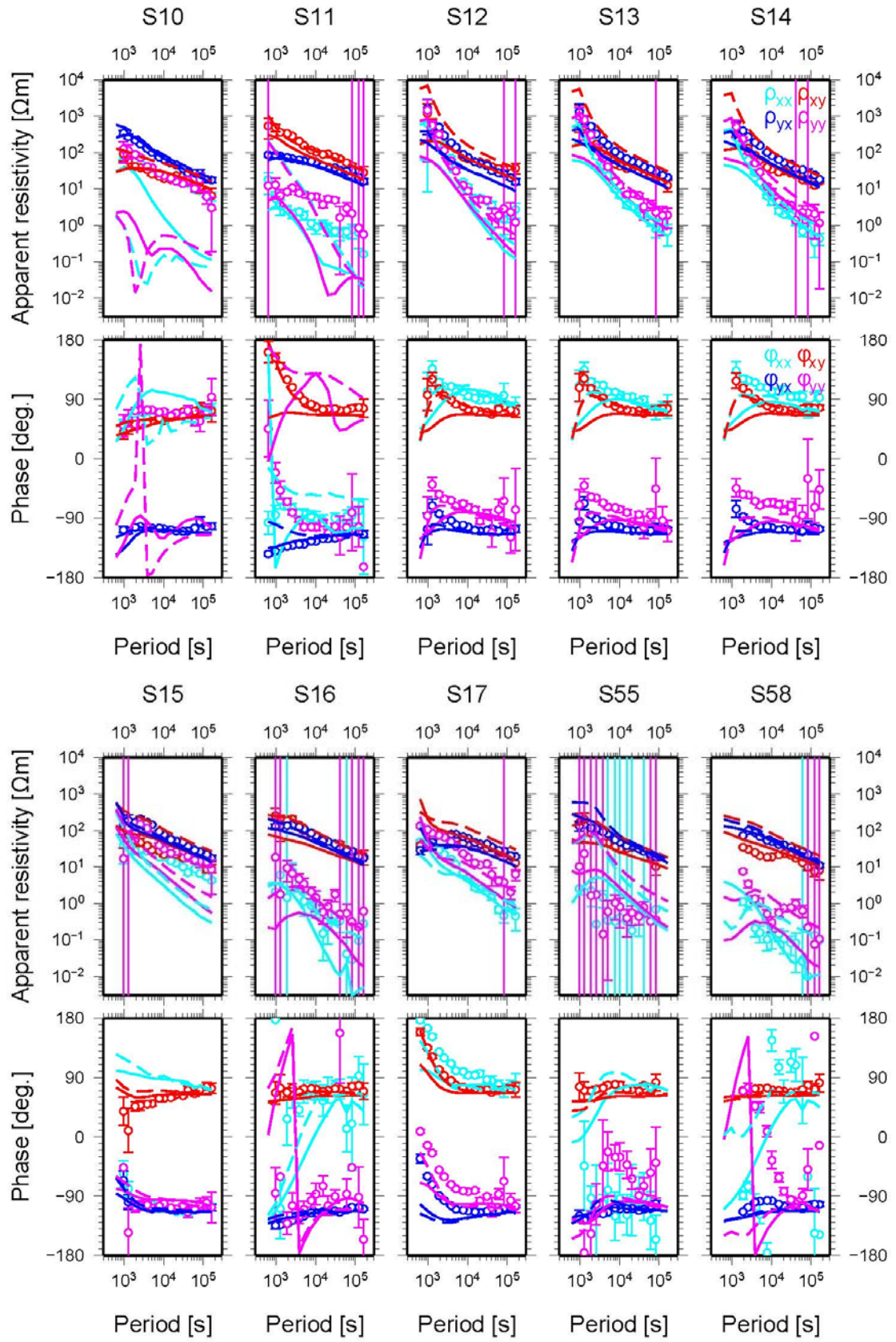
Figure S3. Frequency dependence of all four elements of MT apparent resistivity and phase responses at each site. Symbols with error bars are observed values. Dashed and solid lines are calculated from the initial and final models, respectively. RMS data misfit at each site are shown in Table S3.

Site	Latitude	Longitude	Depth (m)
SOC1	19°28.09′S	148°02.99′W	4427
SOC2	20°57.37′S	146°26.53′W	4773
SOC3	19°55.71′S	146°01.56′W	4656
SOC4	18°25.69′S	144°59.27′W	4477
SOC5	17°30.07′S	144°30.41′W	4049
SOC6	18°48.33′S	142°17.77′W	4507
SOC7	19°56.43′S	142°41.29′W	4490
SOC8	20°57.29′S	143°45.42′W	4806
SOC9	22°10.05′S	144°41.79′W	4540
S55	17°47.58′S	146°52.26′W	4159
S58	18°34.98′S	147°24.84′W	4377

Table S1. Information on the EM Sites of the TIARES project

	RMS_i	S_i^2	F
Inverted model	5.35	77853.2	-
0.03 S/m	5.73	89274.3	1.15

Table S2. Summary of the one-sided F-test. $F_{0.95} = 1.07$

Site	Diagonal RMS	Off-diagonal RMS	Total RMS
SOC1	3.21 (4.61)	5.01 (2.28)	4.21 (3.64)
SOC2	1.42 (1.39)	2.54 (2.08)	2.06 (1.77)
SOC3	6.49 (3.52)	4.58 (3.92)	5.62 (3.73)
SOC4	5.15 (7.20)	3.53 (5.82)	4.41 (6.55)
SOC5	7.37 (7.83)	2.99 (6.79)	5.62 (7.33)
SOC6	3.41 (5.59)	3.80 (4.44)	3.61 (5.05)
SOC7	3.71 (6.39)	3.09 (4.01)	3.41 (5.34)
SOC8	4.64 (7.40)	3.43 (3.96)	4.08 (5.94)
SOC9	4.37 (3.53)	2.58 (2.85)	3.59 (3.21)
S06	2.57 (3.05)	4.33 (5.58)	3.56 (4.50)
S10	10.28 (11.38)	2.45 (5.04)	7.47 (8.80)
S11	6.51 (11.07)	6.51 (6.13)	6.51 (8.94)
S12	4.40 (2.90)	6.20 (7.19)	5.38 (5.48)
S13	3.83 (2.37)	6.54 (9.69)	5.36 (7.06)
S14	4.07 (3.90)	5.65 (9.10)	4.92 (7.00)
S15	11.70 (12.49)	3.84 (8.09)	8.71 (10.52)
S16	2.11 (1.62)	4.85 (3.08)	3.74 (2.46)
S17	7.91 (5.95)	10.97 (11.92)	9.56 (9.42)
S55	3.06 (6.73)	2.88 (6.99)	2.97 (6.86)
S58	4.55 (6.70)	6.41 (17.82)	5.56 (13.46)
Total	5.66 (6.57)	5.02 (7.32)	5.35 (6.95)

Table S3. RMS data misfit at each site for the final model. Figures in the brackets are misfits for the initial model.

References

Baba, K., N. Tada, H. Utada, and W. Siripunvaraporn (2013), Practical incorporation of local and regional topography in three-dimensional inversion of deep ocean magnetotelluric data, *Geophysical Journal International*, *194*(1), 348-361, doi:10.1093/gji/ggt115.

Dasgupta, R., M. M. Hirschmann, and N. D. Smith (2007), Water follows carbon: CO2 incites deep silicate melting and dehydration beneath mid-ocean ridges, *Geology*, *35*(2), 135-138, doi:Doi 10.1130/G22856a.1.

Dasgupta, R., A. Mallik, K. Tsuno, A. C. Withers, G. Hirth, and M. M. Hirschmann (2013), Carbon-dioxide-rich silicate melt in the Earth's upper mantle, *Nature*, *493*(7431), 211-U222, doi:Doi 10.1038/Nature11731.

Gardés, E., F. Gaillard, and P. Tarits (2014), Toward a unified hydrous olivine electrical conductivity law, *Geochemistry, Geophysics, Geosystems*, *15*(12), 4984-5000, doi:10.1002/2014gc005496.

Hashin, Z., and S. Shtrikman (1962), A Variational Approach to Theory of Effective Magnetic Permeability of Multiphase Materials, *J Appl Phys*, *33*(10), 3125-3131, doi:Doi 10.1063/1.1728579.

Hirschmann, M. M. (2010), Partial melt in the oceanic low velocity zone, *Physics of the Earth and Planetary Interiors*, *179*(1-2), 60-71, doi:DOI 10.1016/j.pepi.2009.12.003.

Minarik, W. G., and E. B. Watson (1995), Interconnectivity of Carbonate Melt at Low Melt Fraction, *Earth and Planetary Science Letters*, *133*(3-4), 423-437, doi:Doi 10.1016/0012-821x(95)00085-Q.

Sifré, D., E. Gardés, M. Massuyeau, L. Hashim, S. Hier-Majumder, and F. Gaillard (2014), Electrical conductivity during incipient melting in the oceanic low-velocity zone, *Nature*, *509*(7498), 81-85, doi:10.1038/nature13245.

Siripunvaraporn, W., G. Egbert, Y. Lenbury, and M. Uyeshima (2005), Three-dimensional magnetotelluric inversion: data-space method, *Physics of the Earth and Planetary Interiors*, *150*(1-3), 3-14, doi:10.1016/j.pepi.2004.08.023.

Tada, N., K. Baba, W. Siripunvaraporn, M. Uyeshima, and H. Utada (2012), Approximate treatment of seafloor topographic effects in three-dimensional marine magnetotelluric inversion, *Earth, Planets and Space*, *64*(11), 1005-1021, doi:10.5047/eps.2012.04.005.